Title

Multiscale modeling shows how 2’-deoxy-ATP rescues ventricular function in heart failure

Journal

Proceedings of the National Academy of Sciences of the United States of America, 121(35)

ISSN

0027-8424

Authors

Teitgen, Abigail E

Hock, Marcus T

McCabe, Kimberly J

et al.

Publication Date

2024-08-27

DOI

10.1073/pnas.2322077121

Peer reviewed

PNAS RESEARCH ARTICLE | BIOPHYSICS AND COMPUTATIONAL BIOLOGY

Multiscale modeling shows how 2'-deoxy-ATP rescues ventricular function in heart failure

Abigail E. Teitgen[a], Marcus T. Hock[a], Kimberly J. McCabe[b], Matthew C. Childers[c], Gary A. Huber[d], Bahador Marzban[e], Daniel A. Beard[e], J. Andrew McCammon[d,1], Michael Regnier[c], and Andrew D. McCulloch[a,f,1]

Affiliations are included on p. 10.

Contributed by J. Andrew McCammon; received December 19, 2023; accepted July 22, 2024; reviewed by Gregory Bowman and Michael J. Greenberg

2'-deoxy-ATP (dATP) improves cardiac function by increasing the rate of crossbridge cycling and Ca^{2+} transient decay. However, the mechanisms of these effects and how therapeutic responses to dATP are achieved when dATP is only a small fraction of the total ATP pool remain poorly understood. Here, we used a multiscale computational modeling approach to analyze the mechanisms by which dATP improves ventricular function. We integrated atomistic simulations of prepowerstroke myosin and actomyosin association, filament-scale Markov state modeling of sarcomere mechanics, cell-scale analysis of myocyte Ca^{2+} dynamics and contraction, organ-scale modeling of biventricular mechanoenergetics, and systems level modeling of circulatory dynamics. Molecular and Brownian dynamics simulations showed that dATP increases the actomyosin association rate by 1.9 fold. Markov state models predicted that dATP increases the pool of myosin heads available for crossbridge cycling, increasing steady-state force development at low dATP fractions by 1.3 fold due to mechanosensing and nearest-neighbor cooperativity. This was found to be the dominant mechanism by which small amounts of dATP can improve contractile function at myofilament to organ scales. Together with faster myocyte Ca^{2+} handling, this led to improved ventricular contractility, especially in a failing heart model in which dATP increased ejection fraction by 16% and the energy efficiency of cardiac contraction by 1%. This work represents a complete multiscale model analysis of a small molecule myosin modulator from single molecule to organ system biophysics and elucidates how the molecular mechanisms of dATP may improve cardiovascular function in heart failure with reduced ejection fraction.

dATP | multiscale modeling | cardiac function | myosin | sarcomere

Significance

Myosin activators can improve cardiac function in heart failure with reduced ejection fraction. However, it is not fully understood how the molecular effects of these drugs lead to improvements in ventricular function. We used a multiscale modeling analysis spanning atom to organ system scales to link the molecular mechanisms of 2'-deoxy-ATP (dATP), a myosin activator, to changes in contraction and relaxation at multiple scales of function. Multiscale modeling allowed us to identify therapeutic mechanisms of dATP at each of these scales, which can be extended to other candidate therapeutics.

The naturally occurring nucleotide 2'-deoxy-ATP (dATP) is a candidate myosin activator that has shown promise for treating heart failure with reduced ejection fraction (HFrEF) (1). dATP has been shown to increase force production in skinned myocardium, to increase shortening in isolated cardiomyocytes, and to improve ventricular function in animal models (1–9). How levels of dATP as low as 1 to 2% of the Adenosine triphosphate (ATP) pool significantly improve muscle contraction is not well-understood (8, 9). In addition to increasing the rate of crossbridge cycling, recent studies in cardiac and skeletal muscle suggest that dATP may also increase the pool of myosin available for crossbridge cycling (10–13). We hypothesize that dATP alters the recruitment dynamics of myosin from the thick filament backbone to more active states and that nearest-neighbor cooperativity leads to increased cardiac muscle force development even when dATP is only a small fraction of total adenine nucleotide content in the cell. Further, our recent simulations suggest that dATP increases sarcoendoplasmic reticulum calcium adenosine triphosphatase (SERCA) pump function, leading to faster Ca^{2+} transient decay (14), which has also been observed previously experimentally (4, 8). This may contribute to faster relaxation of cardiomyocytes postcontraction. It is unclear how the these distinct molecular and cellular mechanisms of dATP integrate into improved ventricular pump function, especially in HFrEF when energy metabolism is typically impaired (15, 16).

Here, we use a combination of multiscale computational models to simulate the effects of dATP on myosin dynamics, using molecular dynamics (MD) and rigid body Brownian dynamics (BD). We investigate the resulting effects on sarcomere kinetics using a spatially explicit Markov state sarcomere model. We then assess how these mechanisms interact with altered myocyte Ca^{2+} handling to enhance contractility and lusitropy, using a model of cardiomyocyte mechanics and Ca^{2+} dynamics. Finally, we assess how these myocyte responses contribute to observed improvements in left ventricular mechanoenergetics and hemodynamics in the normal and failing heart by incorporating

Reviewers: G.B., University of Pennsylvania; and M.J.G., Washington University in St. Louis.

Competing interest statement: A.D.M. is a cofounder of and has equity interests in Insilicomed Inc. and Vektor Medical, Inc. He serves as scientific advisor to both companies. Some of A.D.M.'s research grants have been identified for conflict of interest management based on the overall scope of the project and its potential benefit to Insilicomed Inc. and Vektor Medical, Inc. The author is required to disclose this relationship in publications acknowledging the grant support; however, the research subject and findings reported in this study did not involve the companies in any way and have no relationship with the business activities or scientific interests of either company. The terms of this arrangement have been reviewed and approved by the University of California San Diego in accordance with its conflict of interest policies.

[1]To whom correspondence may be addressed. Email: jmccammon@ucsd.edu or amculloch@ucsd.edu.

This article contains supporting information online at https://www.pnas.org/lookup/suppl/doi:10.1073/pnas.2322077121/-/DCSupplemental.

Published August 22, 2024.

this cardiomyocyte model into a biventricular mechanics and lumped-parameter circulatory system model. This comprehensive multiscale model analysis of the heart can be used to predict organ system scale cardiovascular function from atomic resolution simulations of molecular mechanisms and shows how very low fractions of dATP are able to significantly improve pump function and efficiency in the failing heart. Our modeling approach may additionally be a useful tool to study other sarcomere-targeted small molecule activators and inhibitors.

Results

dATP Alters Prepowerstroke Myosin Dynamics, Increasing Its Affinity for Actin. A combination of molecular modeling techniques were utilized to assess how dATP and ATP differentially affect the prepowerstroke conformation of myosin at a molecular level. Three MD simulations of 2 μs each for ATP–myosin and dATP–myosin were carried out (Fig. 1*A*), and featurization analysis of these MD trajectories was carried out based on structural loops and motifs associated with actin binding based on experimental studies (17–19) (Fig. 2*A*). Time-lagged Independent Component Analysis (tICA) was employed for further dimensionality reduction, and was utilized to construct three-state Markov state models (MSM) for ATP–myosin and dATP–myosin to capture their major conformational dynamics (Fig. 2 *B* and *C* and *SI Appendix*, Figs. S1–S4). Representative conformations from the three states are shown in Fig. 2 *G* and *H*. The stationary distribution of the ATP MSM for states 0, 1, and 2 was 34.1%, 40.7%, and 25.2%, respectively. However, for the dATP MSM, the stationary distribution was 5.00% , 8.17%, and 86.8% for states 0, 1, and 2, respectively, suggesting that dATP–myosin has a lower probability of transitioning to a new conformational substate. Further, based on mean first passage time analysis of the transition times between metastable states, the dATP model shows much more rapid transitions into state 2 as the dominant state, whereas the ATP model has much more balanced kinetic transitions between all of the states (Fig. 2 *E* and *F*). We further found that the overall root mean square fluctuation (RMSF) of the protein was lower for dATP–myosin than ATP–myosin, although fluctuations actually increased at key residues in three important domains (Fig. 2*D*). Overall, this analysis demonstrates that dATP reduces structural fluctuations within the prepowerstroke state in the majority of the protein, potentially acting as a stabilizing agent, while simultaneously increasing fluctuations in disordered regions of the protein such as loop 2 and other key regions. However, it should be noted that this MD-MSM method does not explicitly demonstrate increased stability of the prepowerstroke biochemical state, since these simulations do not capture transition out of the prepowerstroke state.

An ensemble-based approach was used to carry out rigid body BD simulations (Fig. 1*B*) of actomyosin association, with conformations sampled from the metastable states of the MSM. dATP–myosin showed a significantly higher ensemble-averaged crossbridge formation rate than ATP–myosin at all simulated reaction distances, where reaction distance is a parameter in the simulation which defines the distance at which the two molecules are considered to bind (*SI Appendix*, Fig. S1). The previously reported ATP–myosin.actin association rate of 2.50×10^6 M^{-1} s^{-1} based on experimental measurements (20–22) corresponds to a reaction distance of 7.20 Å (indicated by the dashed vertical line in Fig. 2*I*). Using this reaction distance, the predicted association rate for dATP–myosin.actin was 4.78×10^6 M^{-1} s^{-1} (3.98×10^6 to 5.73×10^6 M^{-1} s^{-1} 95% CI). This corresponds to a 1.9-fold increase over ATP–myosin.actin (1.4 to 2.8 fold 95% CI). For reaction distances between 6.5 Å and 10 Å, association rates were 1.54 to 2.13 fold greater for dATP than ATP. Full BD simulation results can be found in *SI Appendix*, Fig. S5.

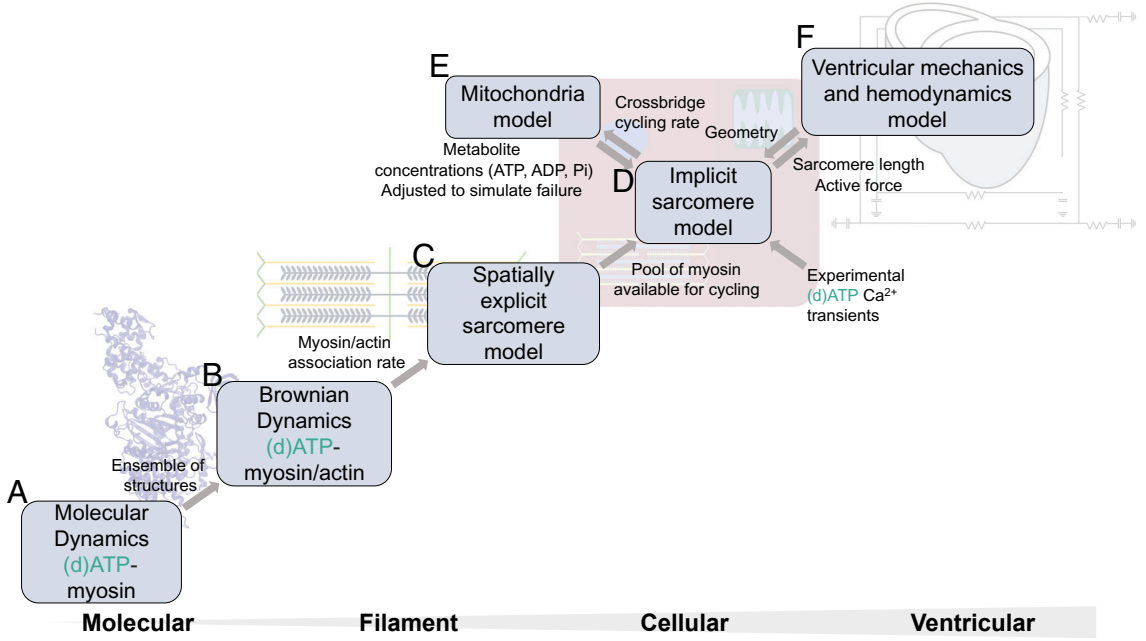

Fig. 1. Multiscale modeling overview. Gray arrows indicate coupling between models. MD simulations of ATP–myosin and dATP–myosin binding to actin (*A*) in combination with BD simulations (*B*) were utilized to determine myosin.actin association rate, which was used to constrain a spatially explicit model of cooperative sarcomere mechanics (*C*). The effects of dATP on myosin predicted by this model were extended to a myocyte model containing an implicit sarcomere mechanics model (*D*), which is driven by experimental Ca^{2+} data, and is coupled to a mitochondrial energetics model (*E*). The myocyte model [(*D* and *E*), and experimental Ca^{2+} data] is embedded within a biventricular mechanics and hemodynamics model of the failing heart (*F*).

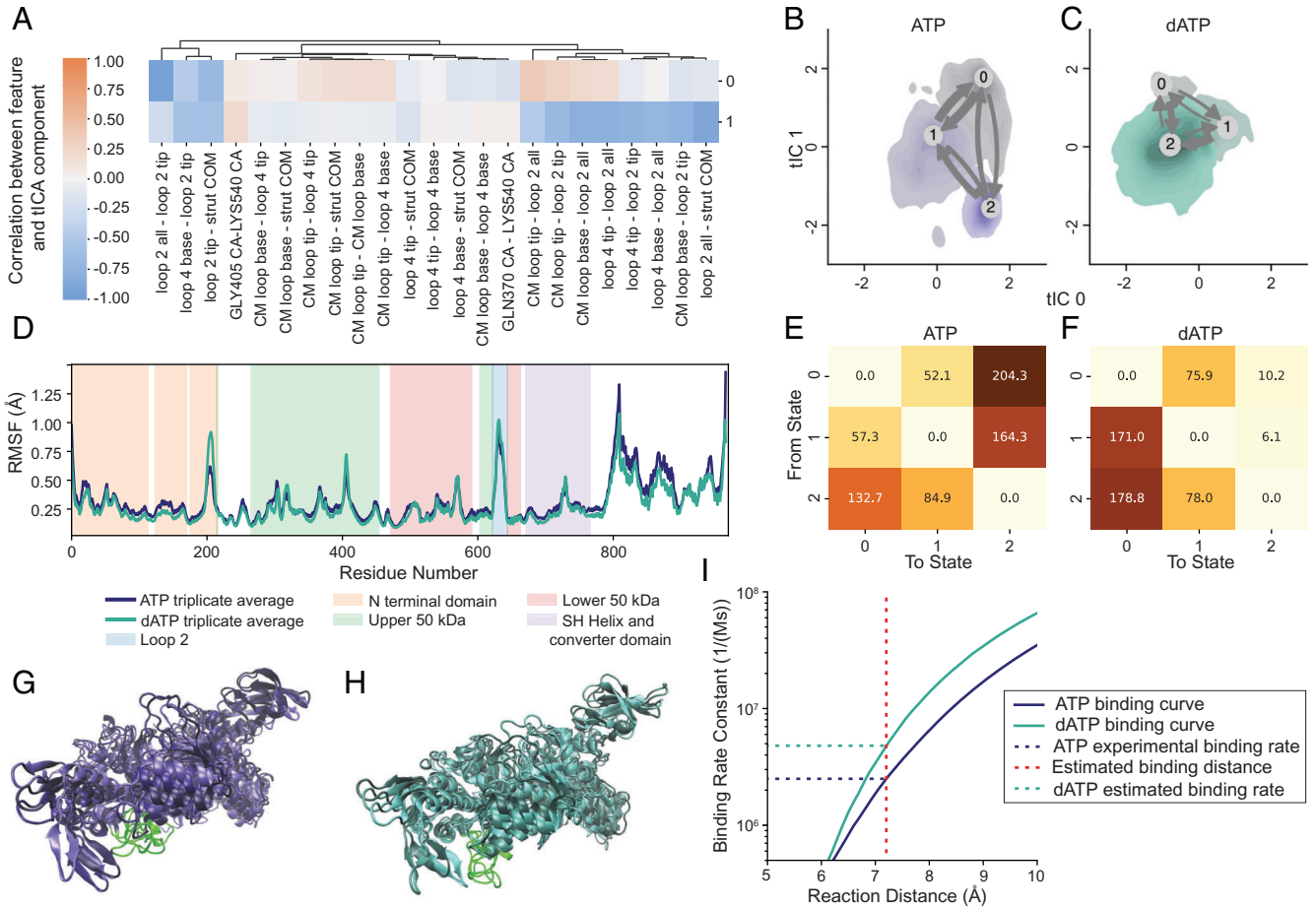

Fig. 2. MD simulations and MSM demonstrate that binding of dATP may stabilize the prepowerstroke myosin head compared with binding of ATP, increasing its affinity for actin. (*A*) Correlation analysis between input features from MD simulations (distances between key structural features on myosin) and first (0) and second (1) tICA components. Clustered with "City-Block" metric. Full region feature descriptions can be found in *SI Appendix*, Fig. S2. Center of mass is abbreviated as COM, and alpha carbons are abbreviated as CA. (*B* and *C*) tICA space visualization of MD simulations, with three metastable states shown for each MSM based on first and second tICA components. Arrows represent flux between states. (*D*) RMSF shown for ATP and dATP, averaged across three MD trajectories for each. Regions of interest on myosin are highlighted. (*E*) Mean first passage times between metastable states shown in (*B*) of ATP-bound myosin simulations (ns). (*F*) Mean first passage times between metastable states shown in (*C*) of dATP-bound myosin simulations (ns). (*G*) Representative conformations from three metastable states for ATP-bound myosin. (*H*) Representative conformations from three metastable states for dATP-bound myosin. Loop 2 is colored in green in (*G* and *H*). (*I*) Binding rate constant estimates of myosin binding to actin using BD simulations.

Increased Force-Dependent Recruitment of Myosin and Nearest-Neighbor Cooperativity Explain Significantly Increased Steady-State Tension Development with Low Fractions of dATP. We next assessed how the predicted increase in actomyosin association affects sarcomere mechanics. Several studies have shown that fractions of dATP as low as 1 to 2% of the ATP pool are sufficient to significantly increase contractile force and shortening (8, 9, 11). We utilized a spatially explicit Markov state sarcomere model (*SI Appendix*, Fig. S6) to assess whether increased actomyosin association could explain these effects with 1% dATP (20, 23) (Fig. 1*C*). After prescribing the ATP–myosin.actin association rate ($k_f^+ = 2.50 \times 10^6\ \mathrm{M}^{-1}\ \mathrm{s}^{-1}$) based on reported measurements (20–22), increasing the actomyosin association rate to $4.78 \times 10^6\ \mathrm{M}^{-1}\ \mathrm{s}^{-1}$ as predicted for dATP–myosin.actin by the BD simulations resulted in a 3% increase in overall sarcomere steady-state force at maximal Ca^{2+} activation (Fig. 3*B*).

A previous study in our group showed using this sarcomere model that dATP increases the crossbridge cycling rate (the powerstroke and crossbridge detachment rates, specifically) in addition to increasing the actomyosin association rate, and that these parameter changes were sufficient to explain experimental changes for simulations with 100% dATP (20). However, increasing parameters k_p^+ (powerstroke rate) and k_g^+ (detachment rate) in addition to k_f^+ by the same amount as in ref. 20 resulted in an 8% increase in steady-state force with 1% dATP (Fig. 3*B*). Experimentally, 100% dATP was shown to increase maximum steady-state force by 31% in demembranated rat cardiac trabeculae (3). Experimental data on changes in steady-state force with 1% dATP are not available, but given data showing that small fractions of dATP are sufficient to significantly increase force production, we would expect a larger increase in force with 1% dATP. This suggests that although our previous modeling results were sufficient to explain the effects of 100% dATP, additional mechanisms must be considered for small fractions of dATP.

We then modified the model to include the active (ON) and inactive (OFF) states of myosin. Transition between these ON and OFF states is governed by parameters k_m^+ and k_m^-, as well as k_{recruit}, which describes the force dependence of this transition (24, 25). We found that increasing parameter k_{recruit} from 0.2 $\mathrm{N}^{-1}\ \mathrm{m}^{-2}$ to 779 $\mathrm{N}^{-1}\ \mathrm{m}^{-2}$, in addition to k_f^+, k_p^+, and k_g^+,

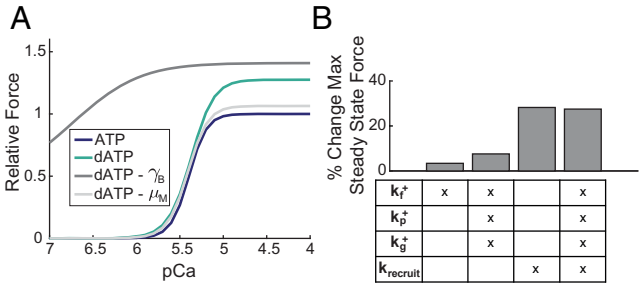

Fig. 3. dATP increases the pool of myosin available for crossbridge cycling, which leads to disproportionate increases in force with 1% dATP. (*A*) Model-predicted force-pCa curves are shown for ATP (purple) and 1% dATP (teal). ATP curve was fit to experimental steady-state force-pCa data from ref. 3. dATP simulation includes increases in actomyosin association rate (k_f^+), powerstroke rate (k_p^+), and detachment rate (k_g^+), as well as increased force-dependent recruitment of myosin ($k_{recruit}$). Effects of setting cooperative parameters γ_B and μ_M to one, thus removing their effects from the model, are also shown. (*B*) Relative contributions of increased crossbridge binding and cycling and increased myosin recruitment to increases in maximum steady-state force (at pCa 4.0) relative to ATP. Differences are expressed as percentages relative to ATP. Full simulation results are shown in *SI Appendix*, Fig. S8.

resulted in a 28% increase in steady-state force with 1% dATP, which was the maximal increase in force that could be achieved and is close to the observed increase of 31% for 100% dATP (Fig. 3 *A* and *B*, additional details found in *SI Appendix*, Figs. S8*A* and S9 and Table S2). $k_{recruit}$ was the only parameter in the model which could be increased to produce such a dramatic increase in steady-state force (*SI Appendix*, Fig. S9). $k_{recruit}$ determines the force dependence of the recruitment of myosin from the thick filament backbone, and is regarded as a mechanism of thick filament mechanosensing (24). Previous computational work (12) showed that dATP activates the resting conformation of cardiac myosin, and X-ray diffraction data (11) and fluorescent assays (13) showed decreases in the fraction of myosin heads in an ordered or low ATPase activity state (respectively) with increased dATP (10). Further, X-ray diffraction data indicate that dATP treatment increases strain in the thick filament backbone, providing support for the idea that dATP leads to recruitment of additional myosin heads via mechanosensing (11). Therefore, our results suggest that dATP-mediated recruitment of myosin to state(s) that can contribute to contraction is the dominant mechanism by which it increases steady-state force, especially at low dATP fractions.

We further assessed whether nearest-neighbor cooperativity could explain this increase in steady-state force with increased myosin recruitment. After increasing k_f^+, k_p^+, k_g^+, and $k_{recruit}$, we set each of the cooperative parameters (γ_B, γ_M, and μ_M) to one, thus eliminating their effects from the model, and assessed their relative impacts on maximum steady-state force. We found that setting γ_B to one resulted in increased steady-state force (41% increase relative to ATP) but flattened the force-pCa curve due to loss of cooperativity via thin filament (tropomyosin) overlap (Fig. 3*A*). Setting μ_M to one resulted in reduced steady-state force (6% increase relative to ATP) due to a loss of cooperativity between neighboring bound crossbridges (Fig. 3*A*). Further analysis of the interaction between dATP and cooperative mechanisms in the model can be found in *SI Appendix*, Figs. S8*B* and S10.

These results support the hypothesis that by increasing the pool of myosin available for crossbridge cycling, a small fraction of dATP can have a disproportionate effect on sarcomere mechanics by promoting the formation of ATP–myosin.actin crossbridges via nearest-neighbor cooperative interactions, both from neighboring bound crossbridges and tropomyosin overlap.

Increased Myosin Recruitment and Calcium Sequestering Dynamics Are Needed to Explain Improvements in Myocyte Contractility and Lusitropy with Elevated dATP. We next utilized an implicit model of sarcomere mechanics and cardiomyocyte Ca^{2+} handling (*SI Appendix*, Fig. S11) to extend these results to the whole myocyte level (Fig. 1*D*). This implicit model was chosen because it is less computationally expensive than the spatially explicit sarcomere model utilized above (Fig. 1*C*), and is more comprehensive in its inclusion of a viscoelastic model, Ca^{2+} dynamics, and coupling to a mitochondria model (Fig. 1*E*) to allow for cell shortening and whole heart mechanoenergetics simulations (Fig. 1*F*). The implicit myocyte model utilized in this study contains an additional crossbridge cycling state (the weakly bound state) (*SI Appendix*, Fig. S11) compared with the spatially explicit model (*SI Appendix*, Fig. S6), and we thus adjusted slightly different crossbridge cycling parameters to achieve the same effect in the implicit model (k_f^+, k_f^-, and k_w^+) as in the spatially explicit model (k_f^+, k_p^+, and k_g^+). Adjusting these parameters (k_f^+, k_f^-, and k_w^+) resulted in a good model fit to experimental force-pCa data (3) with 100% dATP (Sum of squares error was 0.1267 for ATP and 0.2089 for dATP), in line with previous results from the spatially explicit model (20). More details on these models, including parameter selection, can be found in *Materials and Methods* and *SI Appendix*, Tables S2 and S3.

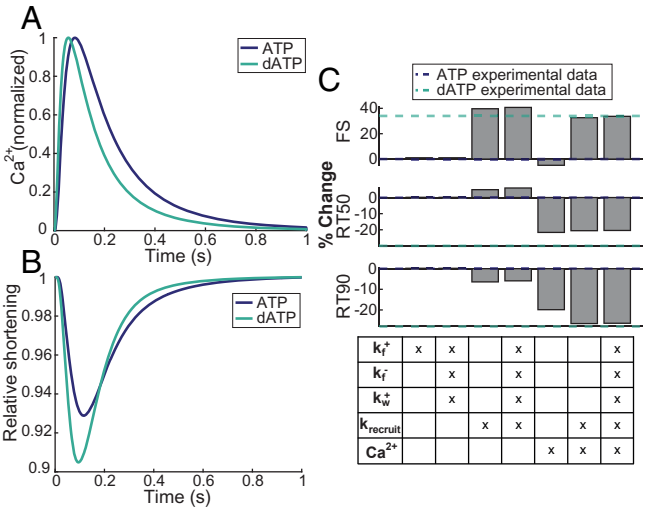

Fig. 4. Increased myosin recruitment and Ca^{2+} sequestering dynamics are needed to explain improvements in myocyte contractility and lusitropy with elevated dATP. (*A*) Model-simulated Ca^{2+} transients for ATP (purple) and dATP (teal), based on average experimental data from refs. 4 and 8. (*B*) Cell shortening simulations for ATP (purple) and 1% dATP (teal), including increased crossbridge binding (increasing k_f^+) and cycling (increasing k_f^- and k_w^+), faster Ca^{2+} dynamics [shown in (*A*)], and increased myosin recruitment (increasing $k_{recruit}$). (*C*) Relative contributions of increased crossbridge binding and cycling, faster Ca^{2+} dynamics, and increased myosin recruitment to changes in FS, RT50, and RT90 compared with average experimental data from refs. 4 and 8. Baseline experimental ATP values are shown as purple dashed lines, and experimental dATP values are shown as teal dashed lines. Differences are expressed as percentages relative to ATP. Full simulation results are shown in *SI Appendix*, Fig. S15.

We found that increasing the ATP–myosin.actin association rate, k_f^+, from 2.50 × 10^6 M^{-1} s^{-1} to 4.78 × 10^6 M^{-1} s^{-1} in the myocyte model based on the BD results resulted in only a 1% increase in fractional shortening (FS) with 1% dATP, consistent with our findings using the spatially explicit model (Fig. 4*C*). Similarly, increasing parameters k_f^- (actomyosin detachment rate) and k_w^+ (weakly to strongly bound transition rate) in addition to k_f^+ did not further increase FS (Fig. 4*C*). However, as was the case at the filament scale, we found that increasing parameter $k_{recruit}$ from 0.2 N^{-1} m^{-2} to 37 N^{-1} m^{-2} in addition to k_f^+, k_f^-, and k_w^+ resulted in a 41% increase in FS with 1% dATP (Fig. 4*C* and *SI Appendix*, Table S3), greater than the experimentally measured increase of 34%. Again, this was the only parameter which could produce this effect (*SI Appendix*, Fig. S16). This further supports the conclusion that dATP treatment leads to disproportionate increases in force with 1% dATP by disrupting the resting states of myosin, which outweighs the effects of increased crossbridge binding and cycling. However, increased recruitment of myosin with elevated dATP resulted in slowed time to 50% relaxation (RT50) and only explained 21% of the experimental change in time to 90% relaxation (RT90) (4, 8). (Fig. 4*C*), so we next sought to assess additional factors that could explain these changes in relaxation.

When the effects of 1% dATP (99% ATP) on the Ca^{2+} transient were simulated by prescribing the average experimental dATP Ca^{2+} transient, which showed decreased time to 50% and 90% Ca^{2+} transient decay (DT50 and DT90, respectively) relative to the 100% ATP transient (4, 8) (Fig. 4*A*), RT50 was decreased by 22% and RT90 was decreased by 20%, which is closer to the experimental data (4, 8) (Fig. 4*C*). When the more rapid Ca^{2+} dynamics with elevated dATP were combined with increased myosin recruitment from resting states, as described above, these mechanisms together explained 97% of the average experimental increase in FS, 70% of the experimental increase in RT50, and 96% of the experimental increase in RT90 (Fig. 4 *B* and *C*). Additionally, including increased rates of crossbridge binding and cycling with elevated dATP in addition to increased myosin recruitment and faster Ca^{2+} transient decay did not substantially change FS, RT50, or RT90 (Fig. 4*C*). These results are further described in *SI Appendix*, Fig. S15.

Therefore, our model predictions suggest that the integrative mechanisms of dATP on myosin recruitment and Ca^{2+} sequestering dynamics can explain improved contractility and lusitropy with elevated dATP at the myocyte level, as well as the high sensitivity of cardiac muscle to small fractions of dATP.

Increased Myosin Recruitment with Elevated dATP Contributes to Improved Ventricular Mechanoenergetics. In animal models, the ventricular concentration of dATP has successfully been increased via upregulation of the enzyme ribonucleotide reductase (R1R2), which converts ADP to dADP (1). dADP is then converted to dATP by the normal cellular rephosphorylation process. Elevated dATP has been observed to significantly increase left ventricular developed pressure (LVdevP), cardiac output (CO), and ejection fraction (EF) in transgenic mice overexpressing R1R2 and infarcted pig hearts treated with R1R2 via an adeno-associated viral vector in vivo (4, 7). Therefore, we next utilized our whole heart and circulation model (*SI Appendix*, Fig. S17) to assess how the predicted effects of dATP on sarcomere and Ca^{2+} dynamics at the myocyte level extend to altered ventricular function. This model contains the

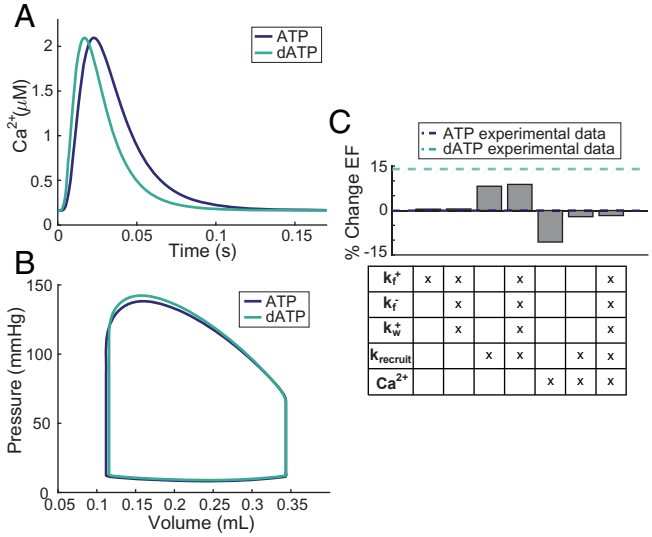

Fig. 5. Increased myosin recruitment leads to improvements in ventricular contractility with elevated dATP. (*A*) Model-simulated average calcium transients for ATP (purple) and dATP (teal), based on experimental data from refs. 4 and 8. (*B*) Pressure volume loops for ATP (purple) and 1% dATP (teal), including increased crossbridge binding (increasing k_f^+) and cycling (increasing k_f^- and k_w^+), faster Ca^{2+} dynamics [shown in (*A*)], and increased myosin recruitment (increasing $k_{recruit}$). (*C*) Relative contributions of increased crossbridge binding and cycling, faster Ca^{2+} dynamics, and increased myosin recruitment to changes in EF compared with experimental data from ref. 4. Baseline experimental ATP values are shown as purple dashed lines, and experimental dATP values are shown as teal dashed lines. Differences are expressed as percentages relative to ATP. Full simulation results are shown in *SI Appendix*, Fig. S19.

same implicit sarcomere and Ca^{2+} handling models utilized for myocyte level simulations (Fig. 1*D*), which are further coupled to a mitochondria model (Fig. 1*E*) and embedded within a biventricular mechanics and hemodynamics model (Fig. 1*F*), as described in *Materials and Methods*.

After adjusting parameters K_{SE}, $k_{passive}$, η, k_{on}, C_{Ao}, and Am_{ref} in the baseline ventricular model to match experimentally measured EF in mice (4) (all other parameters were kept the same as in the myocyte model), we simulated dATP treatment in the same way as in the myocyte shortening simulations (*SI Appendix*, Table S3). We found that increasing k_f^+ from 2.50 × 10^6 M^{-1} s^{-1} to 4.78 × 10^6 M^{-1} s^{-1} in the ventricular model based on the BD results led to a <1% increase in EF, and increasing k_f^- (actomyosin detachment rate), and k_w^+ (weakly to strongly bound transition rate) did not further increase EF (Fig. 5*C*). Consistent with our results at the filament and myocyte scales, we found that increasing $k_{recruit}$ from 0.2 N^{-1} m^{-2} to 37 N^{-1} m^{-2} in addition to k_f^+, k_f^-, and k_w^+ led to a 9% increase in EF, which more closely matches experimental data which showed a 14% increase in EF with dATP (4) (Fig. 5*C* and *SI Appendix*, Fig. S19).

Interestingly, when we included faster Ca^{2+} dynamics in the ventricular model (Fig. 5 *A*–*C*) we observed reduced EF, contrary to our findings at the myocyte scale (Fig. 5*C*). However, these findings are consistent with multiscale modeling results from ref. 26, where increasing the Ca^{2+} reuptake rate into the sarcoplasmic reticulum led to reduced EF. The combined effects of dATP on myosin recruitment and Ca^{2+} sequestering dynamics led to an overall decrease in EF with 1% dATP (Fig. 5 *B* and *C*),

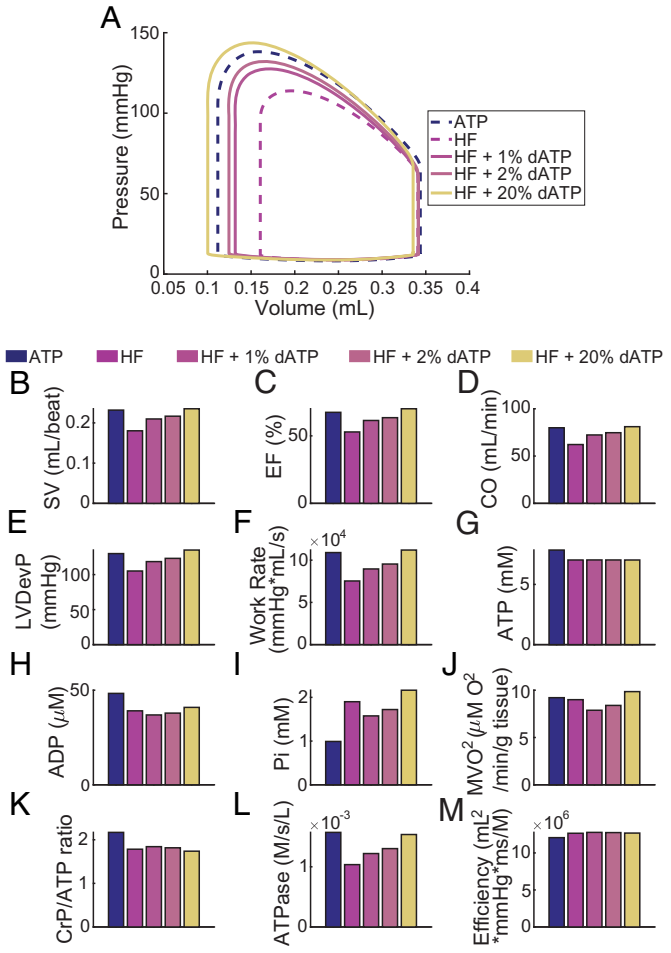

Fig. 6. Elevated dATP leads to improved ventricular function in failing hearts with 1% dATP, and improves energetic efficiency. (*A*) Pressure–volume loops for varying ratios of dATP, including increased myosin recruitment (increasing $k_{recruit}$), crossbridge binding (increasing k_f^+) and cycling (increasing k_f^- and k_w^+), and Ca^{2+} sequestering dynamics with elevated dATP. Baseline ATP healthy heart simulation (fit to data from ref. 4) is shown as a purple dashed line. For HFrEF simulations, the pink dashed line is baseline HFrEF simulation, the yellow line is 20% dATP, and color gradient represents increasing ratios of dATP (1%, 2%, and 20%). Varying dATP percentages were simulated as described in *Materials and Methods*. (*B–M*) Metrics of LV mechanical function and energetics vs. dATP ratio, for the same dATP percentages as in (*A*).

likely due to these Ca^{2+} transient effects. However, these results support the conclusion that increased recruitment of myosin from the thick filament backbone is the primary mechanism by which dATP improves contractility.

Elevated dATP Improves Ventricular Function in the Failing Heart in Part Due to Improved Energetic Efficiency. To simulate HFrEF, the metabolite concentrations in the model were adjusted to mean values previously measured experimentally in failing rat hearts (27) (*SI Appendix*, Table S4). This resulted in reduced EF in line with average experimentally measured EF (27) (Fig. 6 *A* and *C*). Further, ATP and ADP concentrations were decreased and Pi concentrations were increased, consistent with (27) (Fig. 6 *G–I*). We found that with 1% dATP in the failing heart model, EF increased by 16%, CO increased by 16%, and LVDevP increased by 13% (Fig. 6 *C–E*). EF was returned closer to normal with just 1% dATP (61% vs. 67% in the baseline healthy simulation) and was returned to 67% with 7% dATP (Fig. 6*C*). This aligns well with experimental data in pigs which showed a 16% increase in EF with dATP in failing hearts (7). Therefore, the mechanisms identified at the filament (increased recruitment of myosin), and cellular (faster Ca^{2+} dynamics) scales were sufficient to explain experimentally measured changes in EF with 1% dATP in the failing heart.

Overall, dATP improved ventricular function in a dose-dependent manner (Fig. 6). Further, our model was able to predict the effects of varying percentages of dATP on metabolite concentrations and energetic function in the failing heart. ATP levels were unchanged (suggesting that dATP treatment does not substantially deplete ATP pools), while ADP and Pi levels increased with increasing dATP ratio (Fig. 6 *G–I*), as in ref. 4. The creatine phosphate (CrP)/ATP ratio was decreased slightly with increasing dATP ratio (Fig. 6*K*). Further, myocardial oxygen consumption (MVO_2) and ATPase rate also increased with increasing dATP ratio (Fig. 6 *J* and *L*). However, with 1% dATP MVO_2 remained below normal, nonfailing levels. Interestingly, efficiency, defined as the work per beat divided by ATP hydrolysis rate, increased with increasing dATP ratio and was increased by 1% with 1% dATP (Fig. 6*M*). This indicates another potential mechanism by which dATP may improve ventricular function in the failing heart, and could explain why dATP treatment does not lead to further metabolic impairment at low dATP fractions. These results are further described in *SI Appendix*, Figs. S20 and S21.

Finally, we assessed how each of our identified mechanisms of dATP contributed to changes in ventricular function in our normal and failing models. EF, CO, and LVDevP all increased to a greater extent with 1% dATP in failure (16%, 16%, and 13%, respectively) than in the healthy heart simulations, where EF was decreased by 2%, CO was decreased by 2%, and LVDevP was increased by 3% compared to ATP (Fig. 7 *A–C*). Further, these results show that increased myosin recruitment has a larger impact in failure, leading to greater improvements in function. Interestingly, faster Ca^{2+} dynamics with dATP treatment led to increased EF in the failing heart simulations, despite decreasing it in the healthy heart simulations (Fig. 7*A*). Increased myosin recruitment also led to greater increases in work rate (Fig. 7*D*) and efficiency in the failing heart simulations (Fig. 7*H*) (despite decreasing efficiency in the healthy heart simulations), while faster Ca^{2+} dynamics led to an 8% increase in the CrP/ATP ratio (Fig. 7*F*) and a 31% decrease in MVO_2 (Fig. 7*E*) in the failing heart. These findings suggest that the net effect of dATP treatment is to improve contractile function, primarily due to its effects on myosin recruitment, while simultaneously improving energetic efficiency and the overall metabolic state of the failing heart, at least in part due to its effects on Ca^{2+} handling.

Discussion

In this study, we used multiscale computational modeling to integrate therapeutic mechanisms of dATP from the molecular scale to the cardiovascular system in the failing heart. We predicted an increase in the actomyosin association rate with elevated dATP, potentially via overall stabilization of prepower-stroke myosin, as well as increased flexibility in key protein regions. However, we found that this increase, and the resulting enhancement of crossbridge cycling, do not explain significant improvements in contractile function at the myofilament scale and above, particularly when dATP is in low abundance. We found that recruitment of myosin into the crossbridge cycling pool contributed to increases in steady-state force at the filament level, as well as increases in myocyte shortening and ventricular

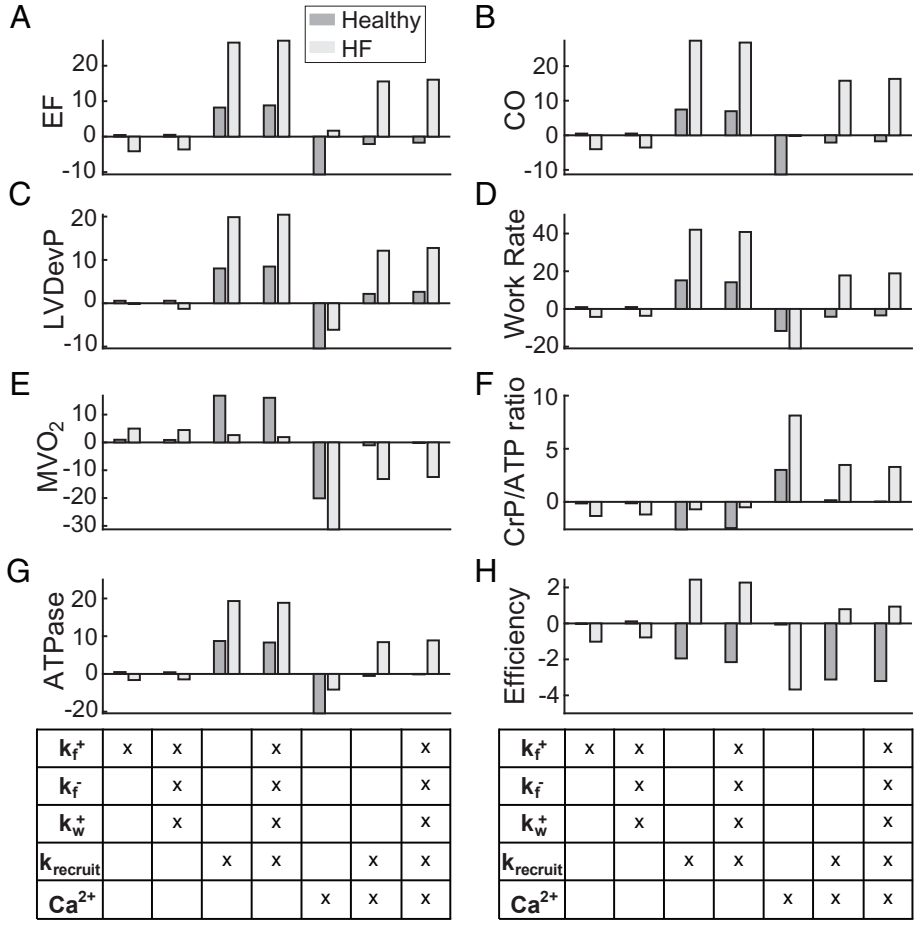

Fig. 7. Elevated dATP improves ventricular function, especially in the failing heart. (*A–H*) Effects of parameter changes on percent change in metrics of LV function and energetics with 1% dATP in healthy and failing heart simulations, shown as percent change compared to ATP. Parameter changes include increased myosin recruitment (increasing k_{recruit}), crossbridge binding (increasing k_f^+) and cycling (increasing k_f^- and k_w^+), and Ca^{2+} sequestering dynamics with elevated dATP.

ejection fraction. Enhanced recruitment of myosin was shown to dominate contractile behavior at all scales, suggesting that this is the primary mechanism by which dATP improves contractility. This illustrates a key advantage of multiscale models, which makes it possible to assess which mechanisms identified at different scales are most important in translating to clinically significant physiological responses. Accounting for the faster Ca^{2+} transient decay observed with elevated dATP along with enhanced myosin recruitment allowed us to also fully explain changes in cellular relaxation, as well as ventricular mechanics in the failing heart. LV function was shown to improve in a dose-dependent manner in simulations of the failing heart, with 1% dATP restoring EF closer to normal levels, in agreement with experimental results. dATP also improved energetic efficiency without further impairing metabolic state in HFrEF simulations. Notably, dATP had a more pronounced impact on ventricular function and energetic efficiency in the failing heart. The multiscale modeling framework developed in this study not only provides a powerful tool for linking molecular effects to changes in ventricular function, but also allowed us to parse the relative effects of several mechanisms of dATP at various scales of function, which would be difficult to accomplish experimentally.

Our modeling approach allowed us to gain mechanistic insight into the effects of dATP on myosin, which agrees well with previous MD simulations (10, 11, 28, 29). While previous myosin MSM have been constructed (30), the MSM-BD framework utilized in this study allowed us to gain insight into the mechanisms by which dATP specifically increases the actomyosin association rate, suggesting a combination of stabilization of the prepowerstroke myosin structure and conformational changes in key protein regions, as well as overall changes in electrostatics. Our hypothesized mechanism of stabilization of the prepowerstroke state of myosin may also decrease the likelihood of transition back into the OFF state, which could be further investigated in future computational studies. Interestingly, our BD simulations showed that dATP increases the actomyosin association rate to a slightly lesser extent than was shown previously (20), although our results were generally consistent (we observed a 1.9 fold change in the association rate compared with a 2.3 fold change in ref. 20). This is likely because our simulations covered a broader range of possible myosin conformations.

Featurization and dimensionality reduction analysis using tICA showed that loop 2 motion was the most important kinetic feature in the MD simulations. Analysis of the input features that influenced BD association rate also showed that the extension of loop 2 away from both the lower and upper 50 kDa domains correlated most strongly with increases in binding rate (*SI Appendix*, Table S1), and warrants further investigation. Specifically, exposure and extension of residues in the tip of loop 2 (GLY-631, GLY-632, LYS-633, and LYS 634) are most

important in the acto-myosin association rate. This aligns with previous work suggesting that switch 1 provides an allosteric mechanism for transmitting changes in the nucleotide-binding pocket to loop 2 and the actin-binding surface, increasing the electrostatic affinity of myosin for actin (12, 31). Further, the metastable conformation that was most dominant in our analysis, state 2 of the dATP simulation, also had the fastest association rate according to our ensemble BD approach (*SI Appendix*, Fig. S5). Generally, all of these structures in state 2 can be described by having a more pronounced loop 2 extension. Even within this subsample of conformations found in state 2, the conformation that associated most quickly according to the BD simulations had an even greater extension of loop 2 relative to the other structures in the state, again pointing to loop 2 as a key structural and electrostatic feature. This analysis also matches with experimental assessments of loop 2 function, which highlight how additional positively charged lysines inserted into the loop increase weak binding (17). Our improved method therefore overcomes a major limitation of BD in which molecules are treated as rigid bodies, by accounting for the conformational variability in several distinct substates, and allowing us to analyze the impact of structural features on protein–protein association.

Our model predictions indicate that thick filament mechanosensing largely contributes to the disproportionate effects of dATP on force. This has been proposed as a mechanism underlying length-dependent activation, where force development coincides with myosin heads transitioning from the thick filament backbone toward thin filaments (11, 24, 32, 33). It is plausible that this may explain how elevated dATP leads to increased recruitment of myosin S1 heads from the thick filament backbone, but the underlying mechanism is still unclear. Furthermore, our model predictions indicated that nearest-neighbor cooperativity was also necessary to explain the large increases in force observed at low dATP percentages, which is consistent with results published in refs. 20 and 24. This may point to a mechanism in which a greater number of myosin heads binding to actin increases the number of exposed myosin binding sites via cooperative mechanisms; this in turn allows more myosin heads to bind and generate force, leading to increased recruitment from the thick filament backbone via a strain-dependent positive feedback mechanism (12, 24). However, it is important to note that myosin can also be recruited from the OFF state via phosphorylation of myosin-binding protein C (34) and the myosin light chain (35), so further investigation is warranted to determine whether these mechanisms may play a role. Further, our results suggest that myosin recruitment is the dominant mechanism by which dATP treatment leads to large increases in force with small amounts (1%) of dATP, while increases in crossbridge binding and cycling were sufficient to explain experimental data with 100% dATP, as shown previously (20). This may be due to the fact that relatively low amounts of dATP may be sufficient to fully deplete the inactive myosin pool. Indeed, recent work showed that with 100% dATP, most myosin heads in the inactive pool have likely been recruited (11, 13). Thus, with 100% dATP, increased crossbridge binding and cycling may be the dominant mechanism by which dATP further increases force production, since all available myosin heads have already been recruited. A combination of experimental techniques and molecular modeling would allow us to fully explore how dATP interacts with nearest-neighbor cooperativity and the inactive state of myosin at varying percentages.

We found that the combined mechanisms of increased myosin recruitment and faster Ca^{2+} dynamics led to both improvements in contractile function and energetic efficiency in the failing heart, while efficiency was decreased in healthy heart simulations. This is consistent with previous findings for Omecamtiv Mecarbil, which has some similar mechanisms to dATP (36). This is likely because in failing conditions, dATP improves both work rate and ATPase rate; however, work rate is increased to a greater extent, leading to an overall increase in efficiency. In the healthy simulations, work rate was decreased, leading to an overall decrease in efficiency. Interestingly, the large improvements in both ventricular function and energetic efficiency in HFrEF were mainly due to increased myosin recruitment into the crossbridge cycling pool. This could plausibly be due to a larger initial pool of myosin heads in inactive states in failure, but additional data are needed to further explore this. We also observed that increased myosin recruitment increased MVO_2 in the healthy heart, but did not increase it as significantly in the failing heart, which may also contribute to improvements in energetics in failure. Further, we observed that faster Ca^{2+} transient decay led to reduced EF in healthy heart simulations but increased EF in failing heart simulations (*SI Appendix*, Figs. S20 and S21), which could be due to the fact that relaxation is likely impaired in failure. Further, we found that dATP increased the CrP/ATP ratio in failure despite not changing it in healthy heart simulations with 1% dATP. Experimental data from healthy transgenic mouse hearts showed a decreased CrP/ATP ratio with elevated dATP (4), but the CrP/ATP ratio has not been measured in HFrEF with dATP, so additional data are needed.

This model provides a powerful tool for assessing the potential therapeutic mechanisms of dATP and integrating existing experimental data spanning molecular to whole organ levels and to generate hypotheses that can be tested through further experimentation and modeling

Limitations

While the modeling framework developed in this study provides insights into the mechanisms by which dATP may reverse contractile dysfunction and could be extended to investigate other small molecule therapeutics, more work will be needed to generalize the present model, which was developed specifically to analyze the effects of dATP on cardiac contractile function. One limitation of multiscale models is the potential that uncertainty can propagate and may amplify across scales; this remains a significant challenge in analyses of this kind.

We chose to utilize two different sarcomere models in this study: a spatially explicit model (20) for filament scale force-pCa simulations, and an implicit model (27) for myocyte shortening and ventricular scale pressure–volume loop simulations. We chose to utilize the spatially explicit model to assess how small fractions of dATP interact with nearest-neighbor cooperativity to produce disproportionate amounts of steady-state force, because this model contains a sophisticated representation of cooperative mechanisms. However, this model is computationally expensive and does not allow for simulation of myocyte shortening, Ca^{2+} dynamics, or energetics, so we chose to utilize the implicit modeling framework developed by Lopez et al. (27) for larger scale simulations. Due to differences in each of these models, the parameter values adjusted in each model differed slightly, mainly due to the addition of a weakly bound state in the implicit model. dATP may also increase the transition between the weakly and strongly bound states, but additional studies are needed to fully address the mechanisms by which dATP increases the rate of crossbridge cycling. Further, it was necessary to increase $k_{recruit}$ by a greater extent in the spatially explicit model than in the implicit model to achieve the same effect. This may be explained by the

fact that overall forces are lower by several orders of magnitude in the spatially explicit model, which represents a single sarcomere, than in the implicit model, which represents a whole cell.

Further, while we were able to estimate an actomyosin association rate from BD simulation results based on the measured ATP–myosin.actin association rate, we observed a range of possible association rates for varying reaction distances. We note that the ensemble binding curve from dATP state 2, which has the largest stationary distribution, also has the fastest binding rate. It is possible that within dATP state 2, conformational variability leads to greater exploration of states to identify a more favorable conformation. However, the variance of binding rates from each of the dATP states is not substantially different, which suggests that the change in measured association rate is not based on conformational exploration. Further, our BD simulations only included a single myosin head and several actin monomers. The accuracy of these simulations could be further improved in the future by including a more complete representation of the thin filament and multiple myosin heads. Adding additional constraints on myosin head movement, rather than allowing it to freely diffuse around the actin filament, would also improve association rate predictions. It is important to emphasize that while the MD and MSM analysis informs our hypothesis that dATP stabilizes prepowerstroke myosin, leading to increases in the actomyosin association rate, this remains a hypothesis based on correlations rather than a direct causal prediction. Additional simulations will be needed to test this mechanism.

Additional work is needed to fully explore the effects of dATP on Ca^{2+} dynamics. The relative changes in DT50 and DT90 of the Ca^{2+} transient with dATP measured in isolated cardiomyocytes (in vitro) at 1 Hz were utilized to scale the Ca^{2+} transient for the ventricular simulations (at 7 Hz). This does not take into account possible frequency effects on changes to the Ca^{2+} transient with dATP, or the effects of the experimental preparation. Further, we assumed that the changes in the Ca^{2+} transient were independent of dATP fraction, but the validity of this assumption warrants further investigation. Additional work is also needed to determine the underlying mechanism by which dATP increases the rate of Ca^{2+} transient decay. We showed in a recent study that dATP acts on SERCA, leading to faster pumping of Ca^{2+} back into the sarcoplasmic reticulum and thus faster Ca^{2+} transient decay, (14, 37) but additional studies are needed to determine whether dATP also acts on other ATPase pumps or mechanisms that regulate Ca^{2+} handling in the cell. Extension of our model to include a model of the SERCA pump and other proteins involved in Ca^{2+} handling would allow us to further investigate the effects of dATP on the Ca^{2+} transient. It is possible that there are additional mechanisms at play at the ventricular level such as regulation by the autonomic nervous system that could be taken into account in future studies (38). Additionally, we utilized averaged experimental dATP Ca^{2+} transient data for our simulations, since experimental measurements of the extent of the effect of dATP on Ca^{2+} dynamics vary. To further address this limitation, we carried out a sensitivity analysis where we varied the Ca^{2+} transient input into the model and assessed the impact on myocyte and ventricular function (*SI Appendix*, Figs. S22–S26).

In addition to uncertainty in the Ca^{2+} transient, $k_{recruit}$ was increased by around three orders of magnitude to match the expected increase with 1% dATP in the spatially explicit model, and by around two orders of magnitude in the spatially implicit model. The representation of myosin transition out of the OFF state in this model is fairly simplistic, so it is difficult to determine the exact increase in this parameter caused by elevated dATP without a more structurally relevant representation of myosin ON/OFF state dynamics. The myosin OFF state is an ongoing area of investigation, and the mechanisms by which dATP disrupts the resting conformation of myosin are still not fully understood, but additional experimental and computational studies will aid in improving understanding. Regardless, model results showed that $k_{recruit}$ was the only parameter which could be increased to produce disproportionate increases in force with small amounts of dATP, so while the exact magnitude of this change is unknown, this provides support for the conclusion that this is the primary mechanism by which small amounts of dATP improve contractile function. We also carried out an additional sensitivity analysis (*SI Appendix*, Figs. S22–S26) where we varied $k_{recruit}$ simultaneously with the Ca^{2+} transient to assess how variability in these parameters affects myocyte and ventricular mechanics. Generally, faster Ca^{2+} transient decay leads to decreased FS, RT50, and RT90, while increased $k_{recruit}$ leads to increased FS, RT50, and RT90. At the ventricular level, faster Ca^{2+} transient decay leads to decreased EF, CO, LVDevP, work rate, MVO_2, and ATPase rate, while increasing the CrP/ATP ratio and efficiency. Increasing $k_{recruit}$ has the opposite effect, increasing EF, CO, LVDevP, work rate, MVO_2, and ATPase rate, while decreasing the CrP/ATP ratio and efficiency. However, the effects on efficiency are more variable, especially in HFrEF simulations. These patterns are consistent with our overall conclusions and suggest that the balance between these two mechanisms determines overall changes in behavior. In the future, additional experimental data on Ca^{2+} dynamics, as well as higher-resolution data and simulations on myosin OFF state dynamics will aid in better elucidating these mechanisms and the interplay between them.

Finally, our modeling approach utilized a simplified model of the heart which approximates the left and right ventricles as hemispheres. While this approach allowed us to gain valuable insight into the ways in which dATP affects ventricular performance at a relatively low computational cost, in the future this framework could be extended to capture more realistic geometries. A finite element model of the heart would allow us to incorporate patient-specific geometries and to assess regional changes in mechanics, as well as potential growth and remodeling. In the future, it would be valuable to expand our model to include additional mechanisms of heart failure such as myocyte death in myocardial infarction, changes in excitation–contraction coupling, and spatially varying changes in sarcomere dynamics with mutations in sarcomere proteins. Additionally, dATP treatment may lead to functional and/or morphological changes in mitochondria, so further experimental data and expansion of our model to include these mechanisms would allow for a more complete assessment of the effects of dATP on energetics in failure.

Materials and Methods

Fig. 1 provides an overview of the modeling approach. Code can be found at https://github.com/cmrg-lab/dATP_multiscale_modeling, and was developed in part based on a previously published multiscale rat mechanoenergetics model (25, 27, 36, 39), as well as a spatially explicit sarcomere model developed in our group (20). More detailed methods can be found in *SI Appendix*.

Molecular Dynamics Simulations of ATP–Myosin and dATP–Myosin. We conducted MD simulations of prepowerstroke ADP.Pi–myosin and dADP.Pi–myosin (40) (PDB ID: 1QVI, 2.54 Å resolution) (Fig. 1*A*). Conventional MD simulations were performed in triplicate for 2,000 ns each for ATP and dATP

(12 μs net sampling). All simulations were performed with the Assisted Model Building with Energy Refinement (AMBER) package (41, 42).

Markov State Model Construction. The MD simulations were used to construct two MSM for each of the nucleotide conditions (ATP and dATP) (*SI Appendix*, Fig. S1). tICA was used to reduce 22 features (determined based on the behavior of the actin-binding surface of myosin) to two primary features. The 22 input features and subsequent tICA dimensionality reduction were carried out using a concatenation of both ATP and dATP simulation data. Then, independently for each nucleotide condition, *k*-means clustering was utilized to reduce the MD simulations into 500-state space using these two primary features, which were then further reduced to three metastable states. From each of the three metastable states, 15 frames were sampled to be used in BD simulations. Analysis was carried out using PyEMMA (43).

Brownian Dynamics Simulations of Actomyosin Association. We used rigid body BD simulations to estimate the association rate of prepowerstroke myosin to actin, improving on previous work by using an ensemble of representative structures from the MD trajectories sampled from metastable states in the MSM as described above (Fig. 1*B*). BD simulations were carried out with Browndye 2.0 (44). Rather than define a reaction distance, we simulated BD trajectories without a reaction endpoint and recorded the closest distance between actin and myosin during the trajectory in order to calculate association rates at a range of reaction distance criteria.

Spatially Explicit Sarcomere Model. We modeled the effects of dATP on sarcomere mechanics, incorporating the association rates determined from the BD simulations, by modifying a spatially explicit cooperative model of the sarcomere previously published in our group (Fig. 1*C*) (20). The original model consists of five states; here, we added a sixth state to represent the pool of inactive myosin heads not available for crossbridge cycling (OFF), where the transition out of the OFF state is force-dependent (*SI Appendix*, Fig. S6). This model is stochastic and utilizes Monte Carlo Markov Chain modeling techniques. Analysis was carried out using Python (45) and CUDA (46).

Myocyte Mechanics Model. We assessed the effects of dATP on whole myocyte mechanics using a nonspatially explicit (ordinary differential equation-based) sarcomere and myocyte mechanics model developed by Lopez et al. (27) (Fig. 1*D*). This model consists of six states, and includes the same model of transition between the active and inactive states as the spatially explicit model. This model also includes parallel passive and series elastic springs, and a parallel dashpot, to represent sarcomere viscoelasticity (*SI Appendix*, Fig. S11). Analysis was carried out in matrix laboratory (MATLAB) (47).

Crossbridge Energetics and Mitochondrial Metabolism Model. The mitochondria model implemented in (27) was utilized to simulate myocardial energetics (Fig. 1*E*). Metabolite concentrations in the mitochondria model feed into the myocyte mechanics model. The crossbridge cycling rate from the sarcomere model is used to calculate the ATPase rate, which feeds into the mitochondria model. Analysis was carried out in MATLAB (47).

Ventricular Mechanics and Hemodynamics Model. Ventricular simulations under healthy and failing conditions were carried out using the rat biventricular mechanics and hemodynamics model from ref. 27 (*SI Appendix*, Fig. S17), containing the same implicit sarcomere and energetics model described above. Sarcomere length and active force from the implicit myocyte model feed into the ventricular model, and the recomputed geometry is used to update sarcomere length in the implicit sarcomere model (Fig. 1*F*). A lumped-parameter model was coupled to the biventricular mechanics model to represent the circulatory system. Analysis was carried out in MATLAB (47)

Data, Materials, and Software Availability. Model code, Brownian dynamics simulation files, and molecular dynamics trajectory files can be accessed at (48, 49).

ACKNOWLEDGMENTS. This work was supported by NIH grants GM31749 (to G.A.H.), HL154624 (to D.A.B.), HL128368 and P30 AR074990 (to M.R.), HL137100 (to A.D.M.) and P41 GM103426 (to A.D.M. and J.A.M.) and Wu Tsai Human Performance Alliance and the Joe and Clara Tsai Foundation (to A.D.M.). This material is based upon work supported by the NSF Graduate Research Fellowship Program under Grant Number DGE-2038238 (to A.E.T.), the University of California (UC) President's Dissertation Year Fellowship (to A.E.T.), and an American Heart Association Predoctoral Fellowship award ID 906494 (to M.T.H.). This work used the Extreme Science and Engineering Discovery Environment (XSEDE) resource COMET through allocation TG-MCB200100 (to M.R.). XSEDE was supported by the NSF grant number ACI-1548562. Partial funding for M.C.C. was provided by Award Number T32HL007828 from the National Heart, Lung, and Blood Institute. K.J.M. is supported by the Simula-University of California San Diego-University of Oslo Research and Ph.D. training (SUURPh) program, an international collaboration in computational biology and medicine funded by the Norwegian Ministry of Education and Research. The content is solely the responsibility of the authors and does not necessarily represent the official view of the NIH, the NSF, or other funding agencies. Portions of this work were previously part of the Ph.D. dissertation of A.E.T.

Author affiliations: [a]Department of Bioengineering, University of California San Diego, La Jolla, CA 92093; [b]Department of Computational Physiology, Simula Research Laboratory, Oslo 0164, Norway; [c]Department of Bioengineering, University of Washington, Seattle, WA 98109; [d]Department of Chemistry and Biochemistry, University of California San Diego, La Jolla, CA 92093; [e]Department of Molecular and Integrative Physiology, University of Michigan, Ann Arbor, MI 48109; and [f]Department of Medicine, University of California San Diego, La Jolla, CA 92093

Author contributions: A.E.T., M.T.H., K.J.M., M.C.C., D.A.B., J.A.M., M.R., and A.D.M. designed research; A.E.T., M.T.H., and M.C.C. performed research; K.J.M., G.A.H., B.M., D.A.B., and J.A.M. contributed new analytic tools; and A.E.T., M.T.H., M.C.C., J.A.M., M.R., and A.D.M. wrote the paper.

1. K. S. Thomson *et al*., Translation of cardiac myosin activation with 2-deoxy-ATP to treat heart failure via an experimental ribonucleotide reductase-based gene therapy. *JACC Basic to Transl. Sci.* **1**, 666–679 (2016).
2. M. Regnier, A. J. Rivera, Y. Chen, P. B. Chase, 2-deoxy-ATP enhances contractility of rat cardiac muscle. *Circ. Res.* **86**, 1211–1217 (2000).
3. M. Regnier *et al*., Cross-bridge versus thin filament contributions to the level and rate of force development in cardiac muscle. *Biophys. J.* **87**, 1815–1824 (2004).
4. S. G. Nowakowski *et al*., Transgenic overexpression of ribonucleotide reductase improves cardiac performance. *Proc. Natl. Acad. Sci. U.S.A.* **110**, 6187–6192 (2013).
5. S. D. Lundy *et al*., Cell-based delivery of dATP via gap junctions enhances cardiac contractility. *J. Mol. Cell. Cardiol.* **72**, 350–359 (2014).
6. S. C. Kolwicz *et al*., Aav6-mediated cardiac-specific overexpression of ribonucleotide reductase enhances myocardial contractility. *Mol. Ther.* **24**, 240–250 (2016).
7. S. Kadota *et al*., Ribonucleotide reductase-mediated increase in dATP improves cardiac performance via myosin activation in a large animal model of heart failure. *Eur. J. Heart Fail.* **17**, 772–781 (2015).
8. F. S. Korte *et al*., Upregulation of cardiomyocyte ribonucleotide reductase increases intracellular 2 deoxy-ATP, contractility, and relaxation. *J. Mol. Cell. Cardiol.* **51**, 894–901 (2011).
9. B. Schoffstall, A. Clark, P. B. Chase, Positive inotropic effects of low dATP/ATP ratios on mechanics and kinetics of porcine cardiac muscle. *Biophys. J.* **91**, 2216–2226 (2006).
10. W. Ma *et al*., Myosin dynamics during relaxation in mouse soleus muscle and modulation by 2′-deoxy-ATP. *J. Physiol.* **598**, 5165–5182 (2020).
11. W. Ma *et al*., Structural off/on transitions of myosin in relaxed porcine myocardium predict calcium-activated force. *Proc. Natl. Acad. Sci. U.S.A.* **120**, e2207615120 (2023).
12. J. D. Powers *et al*., Cardiac myosin activation with 2-deoxy-ATP via increased electrostatic interactions with actin. *Proc. Natl. Acad. Sci. U.S.A.* **166**, 11502–11507 (2019).
13. J. Walklate, K. Kao, M. Regnier, M. A. Geeves, Exploring the super-relaxed state of myosin in myofibrils from fast-twitch, slow-twitch, and cardiac muscle. *J. Biol. Chem.* **298**, 101640 (2022).
14. M. T. Hock *et al*., Multiscale computational modeling of the effects of 2′-deoxy-ATP on cardiac muscle calcium handling. *J. Appl. Phys.* **134**, 074905 (2023).
15. F. Wu, E. Y. Zhang, J. Zhang, R. J. Bache, D. A. Beard, Phosphate metabolite concentrations and ATP hydrolysis potential in normal and ischaemic hearts. *J. Physiol.* **586**, 4193–4208 (2008).
16. T. Doenst, T. D. Nguyen, E. D. Abel, Cardiac metabolism in heart failure: Implications beyond ATP production. *Circ. Res.* **113**, 709–724 (2013).
17. P. B. Joel, H. L. Sweeney, K. M. Trybus, Addition of lysines to the 50/20 kDa junction of myosin strengthens weak binding to actin without affecting the maximum ATPase activity. *Biochemistry* **42**, 9160–9166 (2003).
18. M. H. Doran *et al*., Myosin loop-4 is critical for optimal tropomyosin repositioning on actin during muscle activation and relaxation. *J. Gen. Physiol.* **155**, e202213274 (2022).
19. M. Lorenz, K. C. Holmes, The actin-myosin interface. *Proc. Natl. Acad. Sci. U.S.A.* **107**, 12529–12534 (2010).
20. K. J. McCabe *et al*., Predicting the effects of dATP on cardiac contraction using multiscale modeling of the sarcomere. *Arch. Biochem. Biophys.* **30**, 108582 (2020).

21. M. A. Geeves, Dynamic interaction between actin and myosin subfragment 1 in the presence of ADP. *Biochemistry* **28**, 5864–5871 (1989).
22. H. D. White, E. W. Taylor, Energetics and mechanism of actomyosin adenosine triphosphatase. *Biochemistry* **15**, 5818–5826 (1976).
23. S. G. Campbell, F. V. Lionetti, K. S. Campbell, A. D. McCulloch, Coupling of adjacent tropomyosins enhances cross-bridge-mediated cooperative activation in a markov model of the cardiac thin filament. *Biophys. J.* **98**, 2254–2264 (2010).
24. K. S. Campbell, P. M. L. Janssen, S. G. Campbell, Force-dependent recruitment from the myosin off state contributes to length-dependent activation. *Biophys. J.* **115**, 543–553 (2018).
25. B. Marzban, R. Lopez, D. A. Beard, Computational modeling of coupled energetics and mechanics in the rat ventricular myocardium. *Physiome* (2020). https://doi.org/10.36903/physiome.12964970. Accessed 24 September 2020.
26. K. S. Campbell, B. S. Christman, S. G. Campbell, Multiscale modeling of cardiovascular function predicts that end-systolic pressure volume relationship can be targeted via multiple therapeutic strategies. *Front. Physiol.* **11**, 1043 (2020).
27. R. Lopez *et al*., Impaired myocardial energetics causes mechanical dysfunction in decompensated failing hearts. *Function (Oxf.)* **1**, zqaa018 (2020).
28. S. G. Nowakowski, M. Regnier, V. Daggett, Molecular mechanisms underlying deoxy-ADP.Pi activation of pre-powerstroke myosin. *Protein Sci.* **26**, 749–762 (2017).
29. M. C. Childers, M. Geeves, V. Daggett, M. Regnier, Modulation of post-powerstroke dynamics in myosin ii by 2'- deoxy-ADP. *Arch. Biochem. Biophys.* **699**, 108733 (2021).
30. J. R. Porter, A. Meller, M. I. Zimmerman, M. J. Greenberg, G. R. Bowman, Conformational distributions of isolated myosin motor domains encode their mechanochemical properties. *eLife* **9**, e55132 (2020).
31. R. Clark, M. A. Ansari, S. Dash, M. A. Geeves, L. M. Coluccio, Loop 1 of transducer region in mammalian class I myosin, Myo1b, modulates actin affinity, ATPase activity, and nucleotide access. *J. Biol. Chem.* **280**, 30935–30942 (2005).
32. M. Linari *et al*., Force generation by skeletal muscle is controlled by mechanosensing in myosin filaments. *Nature* **528**, 276–279 (2015).
33. K. S. Campbell, Impact of myocyte strain on cardiac myofilament activation. *Pflügers Arch. Eur. J. Physiol.* **462**, 3–14 (2011).
34. S. Ponnam, T. Kampourakis, Microscale thermophoresis suggests a new model of regulation of cardiac myosin function via interaction with cardiac myosin-binding protein C. *J. Biol. Chem.* **298**, 101485 (2022).
35. L. Alamo *et al*., Three-dimensional reconstruction of tarantula myosin filaments suggests how phosphorylation may regulate myosin activity. *J. Mol. Biol.* **384**, 780–797 (2009).
36. S. G. Tewari *et al*., Influence of metabolic dysfunction on cardiac mechanics in decompensated hypertrophy and heart failure. *J. Mol. Cell. Cardiol.* **94**, 162–175 (2016).
37. K. J. McCabe *et al*., Exploring the effects of 2.deoxy-ATP on SERCA 2A using multiscale modeling. *Biophys. J.* **118**, 260a (2020).
38. R. Gordan, J. K. Gwathmey, L. H. Xie, Autonomic and endocrine control of cardiovascular function. *World J. Cardiol.* **7**, 204–214 (2015).
39. S. G. Tewari, S. M. Bugenhagen, B. M. Palmer, D. A. Beard, Dynamics of cross-bridge cycling, ATP hydrolysis, force generation, and deformation in cardiac muscle. *J. Mol. Cell. Cardiol.* **96**, 11–25 (2016).
40. S. Gourinath *et al*., Crystal structure of scallop Myosin S1 in the pre-power stroke state to 2.6 Å resolution: Flexibility and function in the head. *Structure* **11**, 1621–1627 (2003).
41. D. A. Case *et al*., Amber 2023. https://ambermd.org/index.php. Accessed 28 April 2023.
42. R. Salomon-Ferrer, D. A. Case, R. C. Walker, An overview of the amber biomolecular simulation package. *Wiley Interdiscip. Rev. Comput. Mol. Sci.* **3**, 198–210 (2013).
43. M. K. Scherer *et al*., Pyemma 2: A software package for estimation, validation, and analysis of markov models. *J. Chem. Theory Comput.* **11**, 5525–5542 (2015).
44. G. A. Huber, J. A. McCammon, Browndye: A software package for brownian dynamics. *Comput. Phys. Commun.* **181**, 1896–1905 (2010).
45. G. Van Rossum, F. L. Drake, *Python 3 Reference Manual* (CreateSpace, Scotts Valley, CA, 2009).
46. NVIDIA, P. Vingelmann, F. H. P. Fitzek, Cuda, release: 11.7. https://developer.nvidia.com/cuda-toolkit. Accessed 11 May 2022.
47. The MathWorks Inc., Matlab Version: 9.5.0 (R2018b). https://www.mathworks.com. Accessed 18 September 2018.
48. A. E. Teitgen *et al*., Data from "Multiscale modeling shows how 2'-deoxy-ATP rescues ventricular function in heart failure." University of California San Diego Library Digital Collections. https://doi.org/10.6075/J00G3KCC. Deposited 31 July 2024.
49. A. E. Teitgen *et al*., dATP_multiscale_modeling:v1.0.0. Zenodo. https://doi.org/10.5281/zenodo.13137395. Deposited 30 July 2024.